Crustal evolution over the last 2 m.y. at the Mid-Atlantic Ridge OH-1 segment, 35°N

Allegra Hosford,[1] Jian Lin, and Robert S. Detrick

Department of Geology and Geophysics, Woods Hole Oceanographic Institution, Woods Hole, Massachusetts

Abstract. We present the crustal and mantle velocity structure along the strike of the eastern rift mountains at 35°N on the Mid-Atlantic Ridge. These results were obtained by an inversion of ~1800 *Pg/Pn* and ~450 *PmP* travel times and by gravity modeling. As commonly observed at slow spreading mid-ocean ridges, thicker crust (9 km) occurs at the segment midpoint, while thinner crust (7 km) is found toward the segment ends. This along strike variation occurs primarily in the lower crust, which is 7 km thick at the segment center and 4-6 km thick at the segment ends. In contrast, the thickness of the upper crust is relatively constant along strike. At the segment ends, relatively low velocities extend for 10-15 km along strike and from the seafloor to 4 km depth. These low velocities may indicate an attenuated melt supply and/or fracturing and alteration within the shallow to mid-crust. Directly beneath a cluster of three seamounts at the segment center is a region of relatively high velocity (+0.5 km/s) in the mid-crust. This feature may correspond to a frozen magma chamber that fed the overlying volcanoes. A synthesis of these results with those from two companion experiments along the rift valley and the conjugate flank provide a detailed record of crustal accretion and evolution at this segment. Specifically, the crustal velocity structures of each flank are nearly identical, and they exhibit a thinner and 16% faster upper crust than is observed on axis. The lower crust is remarkably similar in all three settings, except for a low-velocity body on axis, which is interpreted as a partially molten zone. The maximum crustal thickness is also similar in all three profiles, but north of the segment center, zero-age crust is nearly 4 km thinner than beneath the eastern flank and 2 km thinner than beneath the western flank. These differences may indicate that segment-centered mantle upwelling varies on a timescale of ~2 m.y.

1. Introduction

The Oceanographer fracture zone and the ridge segment to the immediate south ("OH-1") constitute one of the most thoroughly studied sites on the Mid-Atlantic Ridge (MAR). Previous work includes active- and passive-source seismic experiments [*Fox et al.*, 1976; *Sinha and Louden*, 1983; *Ambos and Hussong*, 1986, *Barclay et al.*, 1998], dredging [*Schreiber and Fox*, 1976], bathymetry, gravity, and magnetic surveying [*Detrick et al.*, 1995; *Deplus et al.*, 1998], submersible reconnaissance [*Gràcia et al.*, 1999], geochemical analyses [*Shirey et al.*, 1987; *Yu et al.*, 1997; *Niu et al.*, 2001], and geodynamic modeling studies [*Magde et al.*, 1997]. Much of the interest in segment OH-1 derives from two features at its midpoint which have been interpreted to indicate a particularly large magma budget compared to other segments: a seamount chain which extends from the rift valley along flow lines in both directions to 8 m.y. old crust [*Deplus et al.*, 1998] and a large-amplitude (~50 mGal), circular mantle Bouguer gravity anomaly (MBA) low [*Detrick et al.*, 1995]. The MBA "bull's-eye" over the center of OH-1 is elongated in an east-west direction, suggesting that crust is thicker than average along a flow line from the segment center; this feature persists in the residual mantle Bouguer

gravity anomaly after an assumed thermal effect is removed [*Detrick et al.*, 1995].

To investigate gravity-inferred crustal thickness variations both along and across isochron, three wide-angle refraction lines were acquired along the strike of segment OH-1. This 1996 cruise aboard the R/V *Maurice Ewing*, termed the Mid-Atlantic Ridge Bull's-eye Experiment (MARBE), was the first major controlled-source seismic experiment on the northern MAR south of the Reykjanes Ridge in over 15 years. In this study we present the crustal and upper mantle seismic velocity structure and crustal thickness along a 70 km long refraction line on 2 m.y. old crust in the eastern rift mountains of OH-1 (Figure 1). We then synthesize the results with two companion OH-1 seismic refraction experiments, one along the rift valley [*Hooft et al.*, 2000] and one on 2 m.y. old crust in the western rift mountains [*Canales et al.*, 2000]. These three experiments at OH-1 provide a record of spatial variations in crustal accretion and evolution over the last 2 m.y.

2. Geologic Setting

The 90 km long OH-1 segment is one of the longest spreading segments on the MAR and is located ~450 km southwest of the Azores triple junction (Figure 1a). The segment's northern end is bordered by the 128 km long Oceanographer fracture zone. The segment's southern end is adjacent to a 35 km long, right stepping non-transform offset (NTO). Spreading occurs symmetrically at a full rate of 22 mm/yr with an azimuth of 100° [*DeMets et al.*, 1990]. Of the 40 MAR spreading segments between 15°N and the Oceanographer fracture zone, OH-1's rift valley is one of the
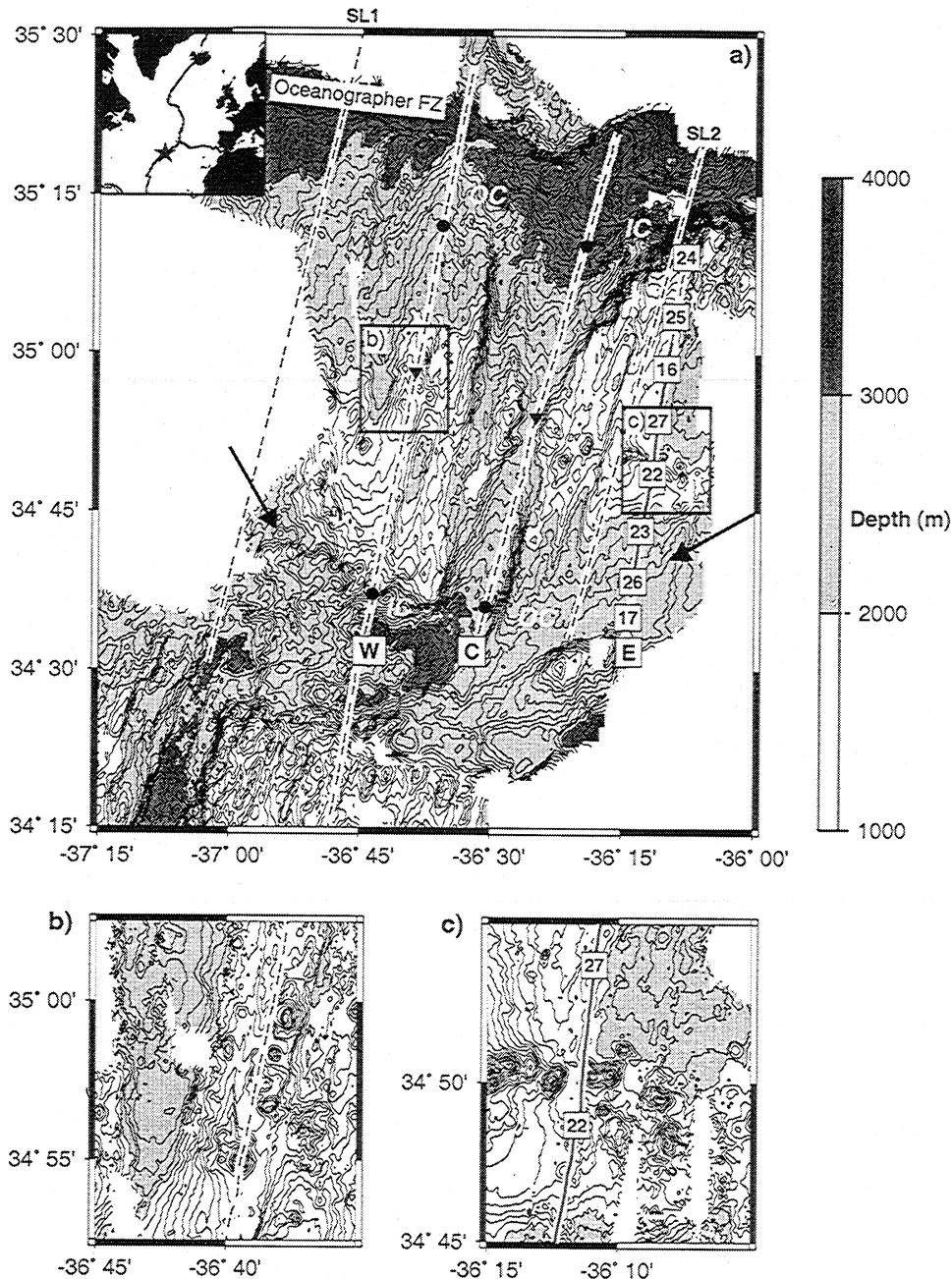

Figure 1. (inset) Location of the study area at 35°N on the Mid-Atlantic Ridge. (a) Bathymetry map of the study area OH-1 gridded at 500 m resolution and contoured every 100 m. Thick white lines with black dashes indicate air gun shot locations for all three refraction experiments at OH-1: Line E on 2 m.y. old crust in the eastern rift mountains (this study), Line C in the central axial valley [see Hooft et al., 2000], and Line W on 2 m.y. old crust in the western rift mountains [see Canales et al., 2000]. Dashed lines labeled "SL1" and "SL2" correspond to lines C1 and B of Sinha and Louden [1983]. Numbered squares denote ocean bottom hydrophone (OBH) locations on Line E. Darkened section of Line E marks the locations of PmP reflections. Solid black circles denote the portions of Lines W and C that are jointly interpreted with Line E. Solid inverted triangles denote position of $x=0$ on Lines W and C in Plates 1 and 2. Arrows indicate propagation wake of OH-1. IC indicates inside corner; OC indicates outside corner. (b) Detail of seamounts along Line W, gridded at 125 m and contoured every 50 m. (c) Detail of seamounts along Line E, gridded at 125 m and contoured every 50 m.

three shallowest, and it has the most negative MBA [*Thibaud et al.*, 1998]. The rift valley is hourglass-shaped in map view. At the segment center the seafloor shoals to 2200 m, and the innermost valley is <3 km wide (Figure 1a). Toward both ends the rift valley deepens and broadens; it is 28 km wide and 3300 m deep at its northern end and 11 km wide and 3000 m deep at its southern end. At the northern end of OH-1 the

eastern and western flanks exhibit the typical topographic asymmetry of inside corners (IC) and outside corners (OC) [e.g., *Severinghaus and Macdonald*, 1988; *Escartín and Lin*, 1995]; the IC adjacent to the fracture zone is 1000 m shallower than the OC. At the southern end the IC adjacent to the NTO is 200 m shallower than the OC (Figure 1a).

The seamounts in the ridge-perpendicular chain at OH-1

appear to differ fundamentally in size and shape from typical MAR valley floor volcanoes. They are large (~115 m average height, 1.5-2 km diameter), form a linear chain in the direction of plate spreading, and appear to survive intact following their formation on axis and subsequent uplift into the flanking crestal mountains and beyond (Figures 1b and 1c) [*Rabain et al.*, 2001]. In contrast, typical MAR rift valley volcanoes are small (~60 m average height, <1 km diameter), isolated or piled on top of one another, and often destroyed or severely disrupted upon uplift from the inner valley [*Smith and Cann*, 1993; *Bryan et al.*, 1994; *Smith et al.*, 1999; *Jaroslow et al.*, 2000].

Like many segments of the MAR [e.g., *Brozena*, 1986; *Carbotte et al.*, 1991; *Gente et al.*, 1992], the length of OH-1 has changed through time. Recent off-axis surveying shows that OH-1 initiated ~15 m.y. ago and propagated southward for 5 m.y. [*Deplus et al.*, 1998]. After a 5 m.y. hiatus, OH-1 again propagated southward to reach its present length of 90 km. This second phase of propagation coincided with the formation of the seamount chain, which at the time of its initiation was located at the southern end of the segment [*Deplus et al.*, 1998]. A prominent V-shaped tectonic scar on the seafloor marks the path of propagation and terminates at the NTO at the southern end of OH-1 (Figure 1a). Within the V-shaped wake, the seafloor is tectonically disturbed, particularly on the western ridge flank.

3. Experiment and Data

This study presents an analysis of seismic and gravity data collected on 2 m.y. old crust within the eastern rift mountains of OH-1, located ~20 km away from the rift valley. The 70 km long seismic refraction profile paralleled the N10°E strike of the spreading center (Figure 1a). Its northern end is located over the IC high south of the Oceanographer fracture zone; the southern end of the seismic line is located on OC crust near the NTO. As part of the same survey, two other refraction profiles were collected at OH-1 (Figure 1a): one within the western rift mountains [*Canales et al.*, 2000] and one within the rift valley [*Hooft et al.*, 2000]. These lines provide a basis of comparison for the results presented here.

The eastern rift mountains of OH-1 comprise several normal-faulted blocks which rise in a stair step fashion from the rift valley [*Gràcia et al.*, 1999]. Water depths at the southern end of the refraction line decrease gradually from ~2500 m at the OC to ~1750 m near the segment center, where the line bisects three seamounts which are 1.5-2 km in diameter and rise 240-430 m above the surrounding seafloor (Figure 1c). North of the seamounts the seafloor along the seismic line remains nearly flat for ~25 km but then rises sharply approaching the IC. The refraction profile ends at ~1200 m water depth, just 10 km south of the 4000 m deep valley of the Oceanographer fracture zone (Figure 1a).

Eight ocean bottom hydrophones (OBH) from the Woods Hole Oceanographic Institution were deployed at an average spacing of 9 km and recorded shots from the 20-gun, 139 L (8495 in^3) air gun array of the R/V *Maurice Ewing*. The array was towed 88 m behind the ship's GPS antenna at a nominal depth of 12 m. Steaming from south to north at ~4.7 knots (0.5 knot = 0.5 m/s), the 120 s firing rate yielded an average shot spacing of 280 m and a total of 265 shots over the length of the line. All seismograms were digitized at a rate of 200 Hz.

Seismic record sections for a subset of the eight receivers are shown in Figure 2. On these record sections, impulsive first arrivals from crustal phases (*Pg*) are visible at offsets <45-50 km; beyond this range the lower-amplitude mantle refraction (*Pn*) crosses over the *Pg* phase to become the first arrival. The *Pg* arrival is not visible within 2 km of each receiver because the direct water arrival obscures crustal

phases; therefore the number of modeled rays which turn in the uppermost 0.5-1 km of crust is low. The Moho reflection (*PmP*), which appears on five of the eight record sections, is identified as a high-amplitude arrival crossing the multiples of the crustal phases (*Pg*) at an oblique angle; Figure 2e illustrates a clear example. The amplitude characteristics and ranges of the three observed phases agree well with the same phases observed in other MAR refraction experiments [*Detrick and Purdy*, 1980; *Sinha and Louden*, 1983; *Purdy and Detrick*, 1986; *Tolstoy et al.*, 1993].

A previous seismic experiment conducted at OH-1 imaged the crustal structure within the eastern rift mountains along a similar transect to the one in this study (Figure 1a) [*Sinha and Louden*, 1983]. Although that experiment used only three sonobouys and 23 shots, the results indicate a relatively normal velocity structure of seismic layers 2 and 3 and a crustal thickness that decreases gradually from a maximum of 9 km at the center of OH-1 to 4-5 km at either end before thinning dramatically beneath the Oceanographer fracture zone. Interestingly, this experiment found that the thinnest crust does not occur beneath the deepest part of the fracture zone valley but, rather, at its northern and southern boundaries [*Louden et al.*, 1986].

The bathymetry map presented in this paper contains data from two sources: Hydrosweep multibeam bathymetry from the R/V *Maurice Ewing* collected during the MARBE cruise and SIMRAD multibeam bathymetry collected on the R/V *L'Atalante* during a cruise in June-July 1991 [*Needham et al.*, 1992]. Free-air gravity data from the two cruises were also merged to produce a combined data set. The MBA was then calculated by removing the predictable gravity effects of the water-crust interface (assuming a density contrast of 1700 kg/m^3) and the crust-mantle interface (assuming a density contrast of 500 kg/m^3 and a 6 km thick crust), following the methods of *Kuo and Forsyth* [1988] and *Lin et al.* [1990].

4. Data Analysis

High-quality seismic data were recorded on six of the eight OBHs; OBH 24 was noisy because it was deployed within the depth range of the SOFAR channel, where acoustic waves are amplified, and OBH 22 was contaminated by instrument noise. To compile the *Pg* and *Pn* travel time data set, we constructed record sections for each instrument by filtering the recorded data between 5 and 40 Hz and picking the first arrivals with an interactive picking program. Application of a spiking deconvolution algorithm greatly facilitated the selection of all arrivals on the two noisy stations and of the low-amplitude *Pn* arrivals on the other stations. Of a maximum 2120 shot-receiver pairs we identified 1810 *Pg* and *Pn* arrivals. Compilation of the *PmP* travel time data set required a lower-frequency band-pass filter (5-12 Hz) due to the lower-frequency content of reflected arrivals. A total of 446 *PmP* travel times were picked on the five receivers on which they were observed.

The *Pg* and *Pn* travel times were assigned picking uncertainties which were used as weights in the tomographic inversion. These picking errors ranged from 10 ms for arrivals with small source-receiver offsets and high signal-to-noise ratios to 40 ms for large offsets and low signal-to-noise ratios. These values are comparable to the picking errors used for the rift valley [*Hooft et al.*, 2000] and western rift mountain studies [*Canales et al.*, 2000], which utilized similar shot-receiver geometry and recorded data of similar quality. The root-mean-square picking uncertainty of all refracted phases was 19 ms. All *PmP* phases were assigned a constant arrival time uncertainty of 50 ms.

The expected fit of a model that fully explains the data is equal to the sum of the variances of the individual sources of
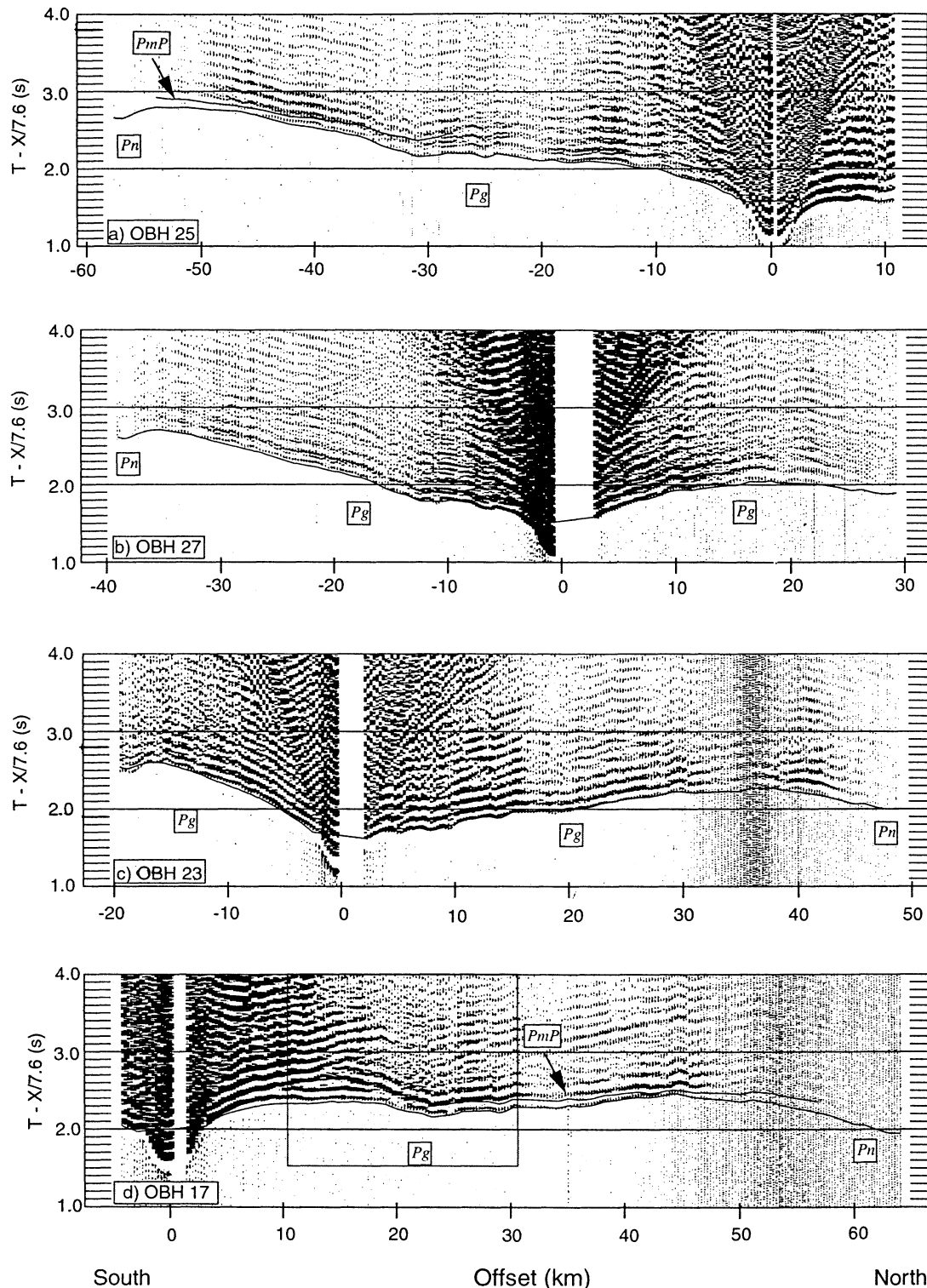
Figure 2. (a-d) Seismic record sections for four of the eight instruments. All record sections are band-pass filtered between 5 and 40 Hz except for Figure 2a, which has been run through a spiking deconvolution algorithm to increase the signal-to-noise ratio. Thin solid lines correspond to the model-predicted travel times and show excellent agreement with picked travel times. Traces are clipped to 1.5 x the trace spacing and are not corrected for topography. The reduction velocity is 7.6 km/s. The Pg (rays refracted in the crust), Pn (rays refracted in the mantle), and PmP (rays reflected off the Moho) phases are labeled. (e) Enlargement of record section for OBH 17 (box in Figure 2d) illustrating high-amplitude PmP arrivals cross-cutting multiples of Pg arrivals.

data error. Additional sources of error in this experiment include uncertainty in source position and in receiver position and depth. We determined these quantities by inverting the travel times of the water column arrival using

the method described by *Creager and Dorman* [1982] (Table 1). While the relocation error ellipses indicate larger uncertainties in receiver position perpendicular to the refraction line than parallel to it, the relocated water depths
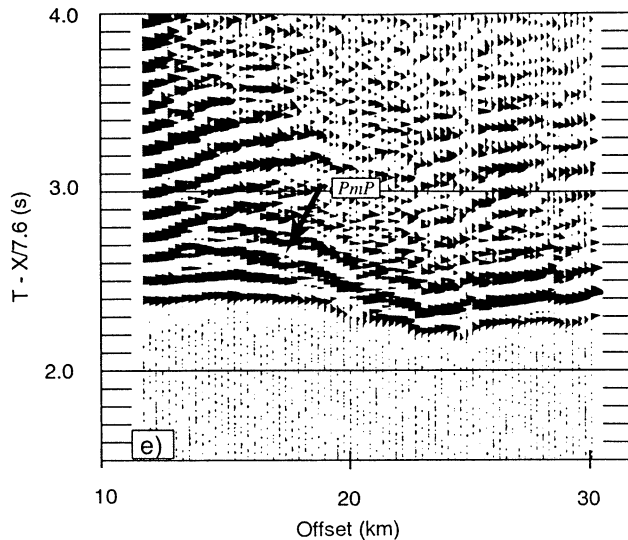
Figure 2. (continued)

differ from the Hydrosweep-derived water depths at the relocated positions by <20 m. The estimated travel time error due to receiver depth uncertainty is 6 ms, and the error due to receiver position uncertainty is 12 ms. The remaining source of experimental error is bathymetry along the refraction line. A common value for vertical depth accuracy in multibeam bathymetry systems is 10 m [McClain and Caress, 1993], which converts to an error of 3 ms in travel time assuming a water velocity of 1.5 km/s and a seafloor velocity of 3 km/s. For this experiment, the root-mean-square uncertainty of all the errors is 23 ms.

5. Inversion Method

The two-dimensional (2-D) tomographic inversion algorithm described by Korenaga et al. [2000] (hereinafter referred to as the Korenaga code) was used to invert the observed travel times for the crustal and mantle velocity structure and Moho depth beneath the eastern rift mountains of OH-1. This code is an iterative method with forward and inverse operations which simultaneously solve for crustal velocities and reflector depth. The ray-tracing step of the modeling procedure occurs via a hybrid scheme that combines the graph method [Moser, 1991] with the ray-bending method [Moser et al., 1992] to produce highly accurate ray paths and travel times [Korenaga et al., 2000]. The inverse step maps the differences between these calculated times and the observed times into perturbations of the initial velocity model. The inversion is stabilized by the addition of user-defined smoothness "correlation lengths," one each in the horizontal and vertical directions for the velocity nodes and one for the depth nodes. All of the smoothing occurs by applying a Gaussian filter of width equal to one correlation length. The removal of travel time residual outliers and the application of post-inversion smoothing also stabilizes the inversion.

The velocity model was parameterized as a 70 km long by 15 km deep grid of nodes. We used a uniform horizontal grid spacing of 1 km and a variable vertical grid spacing which ranged from 100 m at the top of the model to 500 m at its base, for a total of 4446 nodes. The Moho was parameterized at a horizontal node spacing equal to the shot spacing along the line. Based on a series of tests of model regularization we chose a horizontal correlation length for velocity nodes that increased linearly from 5 km at the seafloor to 10 km at the

base of the model, a vertical correlation length for velocity nodes that increased linearly from 0.5 km at the seafloor to 5 km at the base of the model, and a correlation length for reflector nodes of 5 km. For all cases, 10 inversion iterations were performed; most of the variance reduction occurred within the first few iterations.

We tested two starting models for the velocity inversion, one from an experiment south of the Kane fracture zone [Purdy and Detrick, 1986] and one from the MARBE experiment in the rift valley of OH-1 [Hooft et al., 2000]. Each of these velocity structures varied only with depth and were hung from the seafloor bathymetry to form a 2-D grid. While 2-D inversions using these different starting models yielded similar velocity structures and travel time residuals, we chose the velocity profile from the rift valley of OH-1 as the starting model to facilitate comparisons with rift valley crustal structure. For the starting Moho we used the Moho depth obtained by downward continuation of residual mantle Bouguer gravity anomalies along the eastern rift mountain refraction line.

A problem inherent to joint seismic refraction-reflection inversion algorithms is the difficulty in determining the relative contributions of lower crustal velocity changes and variations in Moho depth in producing the PmP travel time residuals [Korenaga et al., 2000]. To explore this ambiguity, a depth kernel weighting parameter is used in the inversion which changes the relative contribution of each of these effects; a factor of 1 corresponds to equal weighting, while a factor >1 favors larger Moho depth perturbations and smaller lower crustal velocity perturbations. For this data set a weighting factor of 1 created large gradients in lower crustal velocities where ray coverage is poor, while a weighting factor >1 produced a velocity model and crustal thickness that are the most consistent with the results from the companion experiments at OH-1 [Canales et al., 2000; Hooft et al., 2000] and with the prior eastern rift mountain experiment [Sinha and Louden, 1983].

6. Results

The P wave velocity structure and Moho depth beneath the eastern rift mountains of OH-1 are presented in Figure 3. The tomographic inversion reduced the root-mean-square (RMS) misfit between the observed and predicted Pg and Pn travel

Table 1. Instrument Positions and Depth

OBH	Latitude, °N	Longitude, °W	Depth Z, km	Position X, km
24	35.1534	36.1289	1.245	29.12
25	35.0603	36.1497	1.829	18.60
16	34.9763	36.1645	2.019	9.17
27	34.8944	36.1777	1.981	0.00
22	34.8194	36.1923	1.852	-9.43
23	34.7206	36.2110	2.204	-19.55
26	34.6414	36.2285	2.420	-28.50
17	34.5852	36.2360	2.581	-34.77

Instrument geographic coordinates were derived using the relocation algorithm of Creager and Dorman [1982]. Depths were obtained from the Hydrosweep bathymetry grid at those relocated positions. The difference between the relocated depths and the Hydrosweep depths is <1%. The choice of ocean bottom hydrophone (OBH) 27 for the coordinate system origin is arbitrary.
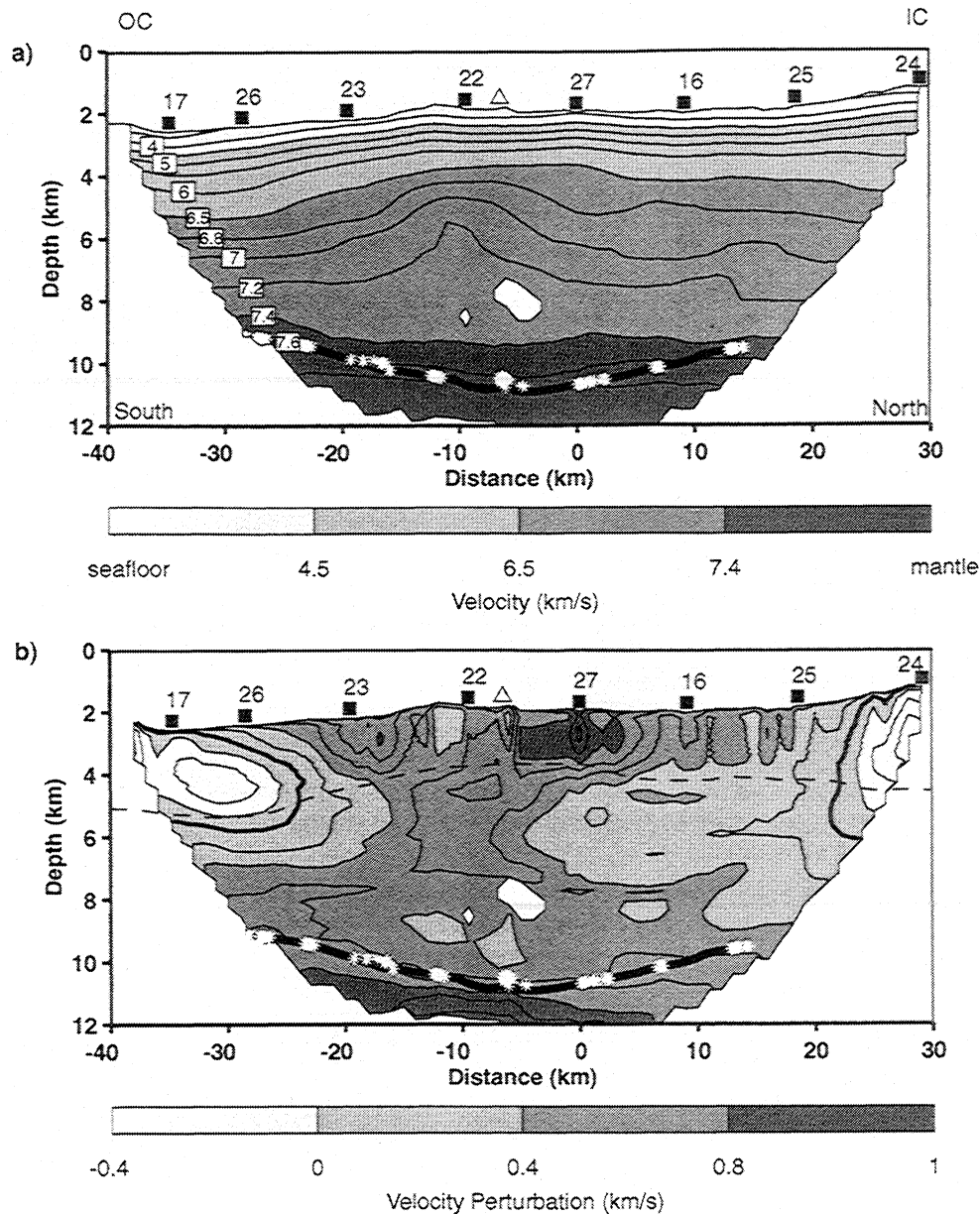
Figure 3. (a) Final *P* wave velocity structure and Moho depth along the eastern rift mountains of OH-1. *PmP* bounce points (white stars) and interpolation between them (thick solid line) define the seismic Moho over the central 45 km of the profile. Velocities are masked where ray coverage is sparse. Solid squares denote instrument locations and the open triangle marks the location of a seamount cluster adjacent to the line. (b) Difference between the final *P* wave velocity model in Figure 3a and an average velocity-depth profile from the central axial valley of OH-1. The dotted line marks the depth of the 6.5 km/s interface and defines the boundary between the upper and lower crust. The thick solid contour emphasizes a velocity perturbation of 0. Vertical exaggeration (VE) is 2.7.

times from an initial value of 172 ms to 30 ms after 10 iterations (Figure 4b). This final travel time residual is comparable to the estimated experimental error of 23 ms. The RMS misfit for the *PmP* travel times decreased from 124 ms for the starting model to 47 ms after 10 iterations (Figure 4c). To illustrate the agreement between the observed and modeled travel times, we overlay the model-predicted travel times on the record sections in Figures 2a-d.

One measure of the spatial resolution of the 2-D velocity structure is the derivative weight sum (DWS) [*Toomey et al.*, 1994], a numerical representation of the "hit count" or ray density near each model grid node. The DWS grid for our

final velocity model indicates that much of the model space is well sampled by turning rays (Figure 4a). The highest DWS values (i.e., the best resolved areas) occur in the mid-crust between 2.5 and 5 km below the seafloor, in the shallow crust immediately beneath each receiver, and in the uppermost mantle. The lowest DWS values (i.e., the least resolved areas) occur at the edges of the model, in the shallow crust between receivers, and in the lowermost crust.

While the DWS array is useful for determining relative regions of high and low ray coverage, it does not account for the angular distribution of rays. We conducted resolution testing to assess the reliability of the inversion results in
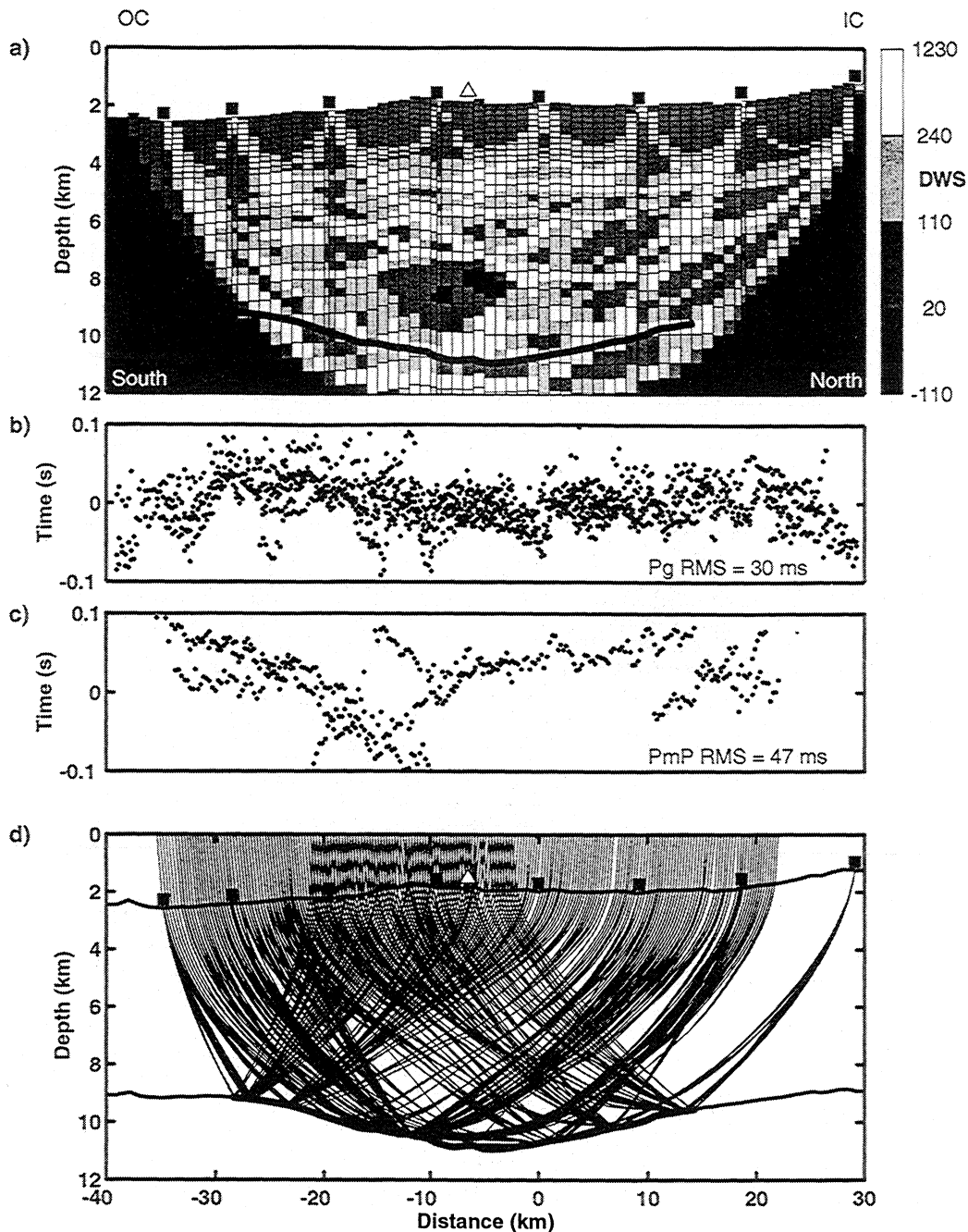
Figure 4. (a) The derivative weight sum (DWS), a measure of refracted ray density, for the final seismic model (Figure 3a). Lighter shading indicates denser ray coverage and better model resolution. No rays pass through black regions. Grid cells indicate model parameterization; for clarity, every other horizontal grid line is shown. Color scale divides the data into quartiles. Thick line indicates Moho. Solid squares denote instrument locations. (b) Travel time residual between observed and model-predicted *Pg* arrivals. Final root-mean-square (RMS) misfit is 30 ms. (c) Travel time residual between observed and model-predicted *PmP* rays. Final RMS is 47 ms. d) *PmP* rays traced through the final seismic model, illustrating the nearly continuous insonification of the Moho over the central 45 km of the line. VE = 2.7.

Figure 3b. Specifically, we wished to test if the regions of high and low velocities in our result were real or artifacts caused by variable ray coverage. In the resolution test, we calculated synthetic travel times for a perturbed velocity model with the same shot-receiver geometry and model parameterization as used for the real modeling. Then we added normally distributed, random noise to the synthetic travel times and inverted them using the initial unperturbed velocity model to determine how well the perturbations were recovered. The synthetic model consisted of a checkerboard pattern of alternating high and low velocities in similar locations as the observed positive and negative anomalies (Figure 5a). Each anomaly measured 15 km wide by 4 km tall and was perturbed by 3% from the background velocity model.

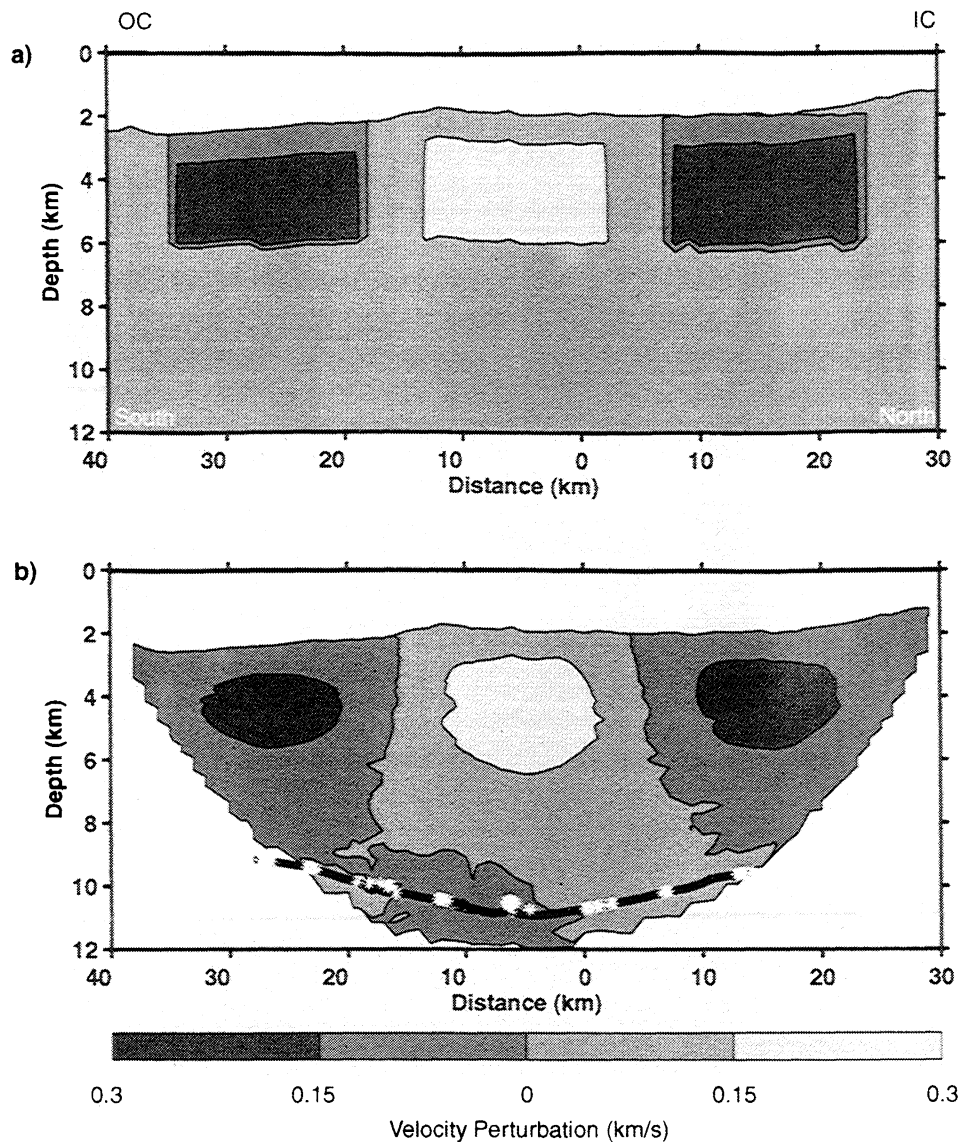The result of the resolution test is shown in Figure 5b.

Figure 5. (a) Synthetic velocity model used to test the resolution of high- and low-velocity bodies in the mid-crust. The velocity perturbation is 3% over the background velocity. (b) Recovered velocity model, using identical inversion parameters and ray paths as in the real experiment. VE = 2.7.

Good recovery was obtained for all three velocity perturbations, with very little vertical and horizontal smearing of the central positive anomaly and some smearing of the distal negative anomalies; this latter effect probably results from the absence of crossing rays at the edges of the model. To confirm that the low-velocity anomalies at the segment ends are not artifacts of the ray coverage, we performed the same resolution test but with perturbations of opposite sign (high velocities at the segment ends and low velocities at the segment center). Again, we recovered the input velocity structure quite well. Based on these results and adequate goodness of fit statistics (RMS = 30 ms, χ^2 = 3.7) we conclude that the inversion results presented in Figure 3b are robustly supported by our data.

6.1. Upper Crust

Absolute velocity values in the upper crust (defined as the depth to the 6.5 km/s contour) agree well with typical seismic layer 2 structure: velocities increase rapidly from 3.5 km/s at

the seafloor to 5 km/s at 1 km depth, then increase more gradually to 6.5 km/s at 3-3.5 km depth (Figure 3a). The thickness of the upper crust varies by ~1 km along the line, with a maximum value of 2.9 km at the southern end and a minimum value of 1.8 km at the center. Immediately beneath OBH 22 and the adjacent seamounts, the upper crust thins locally by ~500 m relative to the surrounding crust. A velocity perturbation plot (Figure 3b) reveals significant lateral heterogeneity in the upper crust relative to the average velocity-depth profile of the central axial valley, which was used as the starting model for the inversion. In particular, we image discrete regions of both anomalously high and low P wave velocities, with the perturbation amplitude spanning 1.2 km/s peak to peak. Two regions of relatively high velocities (+0.5 km/s) are imaged within the shallow crust: one beneath OBH 23 (x=-20 km) and one beneath OBH 27 (x=0 km). In contrast, in between these two regions (x=-10 km), shallow velocities are only slightly higher than velocities in the shallow crust on axis. Each of the high-velocity anomalies extends to 1.5-2 km depth, although these thickness values

may overestimate the real values due to downward smearing by the vertical ray paths beneath receivers.

Two relatively low velocity regions are detected at either end of the seismic profile, as shown in the velocity perturbation field (Figure 3b). These anomalies are lower in overall magnitude than the central high-velocity bodies (-0.1 to -0.5 km/s versus +0.5 km/s), but they extend for greater along-axis distance as well as to greater depth. To the south the negative anomaly is 15 km wide and 4 km thick, and to the north it is at least 10 km wide and 4 km thick. Thus, while the shallower high-velocity bodies at the segment center probably lie wholly within the extrusive section of crust (layer 2A), these lower-velocity regions at the segment ends probably encompass both extrusive and intrusive crust.

Although the uppermost 1-1.5 km of crust is poorly sampled by seismic energy relative to other regions of the model (Figure 4a), the velocities we obtain for the upper crust agree well with the velocity-depth profile obtained from analysis of multichannel seismic (MCS) data in the same area [*Hussenoeder*, 1998]. At 1 km depth, for example, the velocity at x=-18 km and x=5 km is 5 km/s in both the MCS velocity analysis and in our tomographic results.

6.2. Middle and Lower Crust

Middle and lower crustal velocities in our tomographic image correspond to seismic layer 3 values, with velocities increasing from 6.5 km/s at the base of layer 2 to 7.6 km/s at the Moho (Figure 3a). The thickness of layer 3 changes significantly along the profile from 4 km at the southern end to 6 km at the center to 5.5 km toward the northern end. A notable feature in the seismic velocity image (Figure 3a) is the upwarping of the 6.8-7.2 km/s contours in the mid-crust. This high-velocity region measures 6.5 km wide by 2 km tall and is spatially associated with the seamount clusters located on either side of the seismic line (see Figure 1c). The perturbation plot (Figure 3b) shows that the high-velocity body exceeds rift valley velocities over the same depth range by as much as 0.6 km/s, an increase of 7%.

6.3. Moho and Uppermost Mantle

The seismic Moho in the eastern rift mountains of OH-1 is constrained seismically by nearly continuous *PmP* reflections over the central 45 km of the profile (Figures 3a and 4d). Over this distance the crustal thickness is 7 km near the southern end of OH-1, 9 km at the center, and 8 km approaching the northern end. This relatively modest variation in crustal thickness is consistent with the gentle gradient of the overlying seafloor (Figures 1a and 3a), with the relatively small variation in residual gravity along the line (~12 mGal) [*Detrick et al.*, 1995], and with the crustal thicknesses obtained by *Sinha and Louden* [1983]. The maximum crustal thickness of 9 km is larger than typically observed seismically at both the Mid-Atlantic Ridge [e.g., *Purdy and Detrick*, 1986; *Tolstoy et al.*, 1993] and the fast spreading East Pacific Rise (EPR) [e.g., *Caress et al.*, 1992; *Van Avendonk et al.*, 1998].

It is important to note that the *PmP* reflections in this data set were not recorded all the way to the inside corner adjacent to the Oceanographer fracture zone (Figure 1). Thus we cannot confirm with this seismic line alone the inference from gravity data of crustal thinning beneath inside corners [*Escartín and Lin*, 1995]. However, data from the *Sinha and Louden* [1983] experiment indicates that the crust beneath the eastern rift mountains does not thin by more than a few km until within ~10 kilometers on either side of the fracture zone valley.

Because of the thick crust beneath the midpoint of the eastern rift mountains of OH-1, fewer than 20% of the first arrivals on the seismic record sections are *Pn* phases, and consequently, we imaged only the upper 0.5-1 km of the mantle beneath the seismic line. However, this portion of the upper mantle is relatively well resolved by our data set (Figure 4a). The average mantle velocity over the central 30 km of the seismic line ranges between 7.8 and 8.0 km/s. This value is consistent with the apparent *Pn* velocity observed on the record sections (Figure 2), with the results from the seismic line on conjugate crust [*Canales et al.*, 2000], and with the 7.88 km/s mantle velocity obtained by *Sinha and Louden* [1983].

6.4. Density Structure

In the absence of seismic data a common method of estimating crustal thickness and crust and mantle density variations is to calculate the residual mantle Bouguer gravity anomaly (RMBA) [e.g., *Kuo and Forsyth*, 1988; *Lin et al.*, 1990; *Detrick et al.*, 1995]. The seismic model obtained for the eastern rift mountains of OH-1 provides constraints on the sources which contribute to the RMBA. To take maximum advantage of the seismic constraints, we calculate a different residual anomaly, the residual crustal Bouguer anomaly (RCBA), to assess the effect of each of the crustal and mantle sources on the observed gravity signal. To convert the seismic velocity structure to density, we divided the velocity model into sub-blocks with interface boundaries at increments of 0.1 km/s from the seafloor to 7 km/s; this final interface corresponds to the base of the most well-resolved portion of the seismic model. These 2-D interfaces were then extended in three dimensions and hung from the bathymetry within a 3-D volume. The density of each interface was calculated using a density-velocity relation for seismic layer 2 derived by *Carlson and Raskin* [1984], $\rho = 3.5 - 3.79/V_p$, where density ρ is in Mg/m^3 and P wave velocity V_p is in km/s. Finally, the gravity contribution from each interface was calculated by mirroring the density surfaces on all sides and using the *Parker* [1972] Fourier method.

Because we have good resolution in crustal velocities to at least the depth of the 7 km/s velocity contour, we follow the approach of *Canales et al.* [2000] and *Hooft et al.* [2000] to reduce the free-air gravity anomaly to RCBA. The RCBA is obtained by the formula RCBA = FAA − g_{crust} − $g_{thermal}$, where FAA is the observed free-air anomaly, g_{crust} is the sum of the gravity contribution from each density interface from the seafloor to the 7 km/s contour, and $g_{thermal}$ is the gravity effect of the mantle thermal structure based on a passive mantle upwelling model calculated using the approach of *Phipps Morgan and Forsyth* [1988]. The RCBA thus reflects unmodeled crustal and mantle density variations and Moho topography.

Figure 6a illustrates each of the sub-blocks in the density model used to calculate the RCBA. The density gradient is largest in the uppermost crust where seismic velocity increases rapidly; below ~2 km depth, crustal density increases more slowly to the final model density contour of 2950 kg/m^3 (corresponding to 7 km/s). Each successive density interface below the seafloor contributes only a few mGal to the total RCBA. Figure 6b shows that the RCBA retains the general character of the MBA gravity low centered on OH-1 [*Detrick et al.*, 1995]. Over the central 60 km of the line, however, the total amplitude of the RCBA is only 15 mGal, which is half the 30 mGal RCBA variation observed in the axial valley over the same distance [*Hooft et al.*, 2000].

The observed RCBA is compared with the gravity effect of the Moho topography in Figure 6b. Again using the *Parker* [1972] Fourier method, we assume a constant density contrast across the Moho of 350 kg/m^3 (Figure 6a). Since the seismic Moho is obtained only over the central part of the seismic
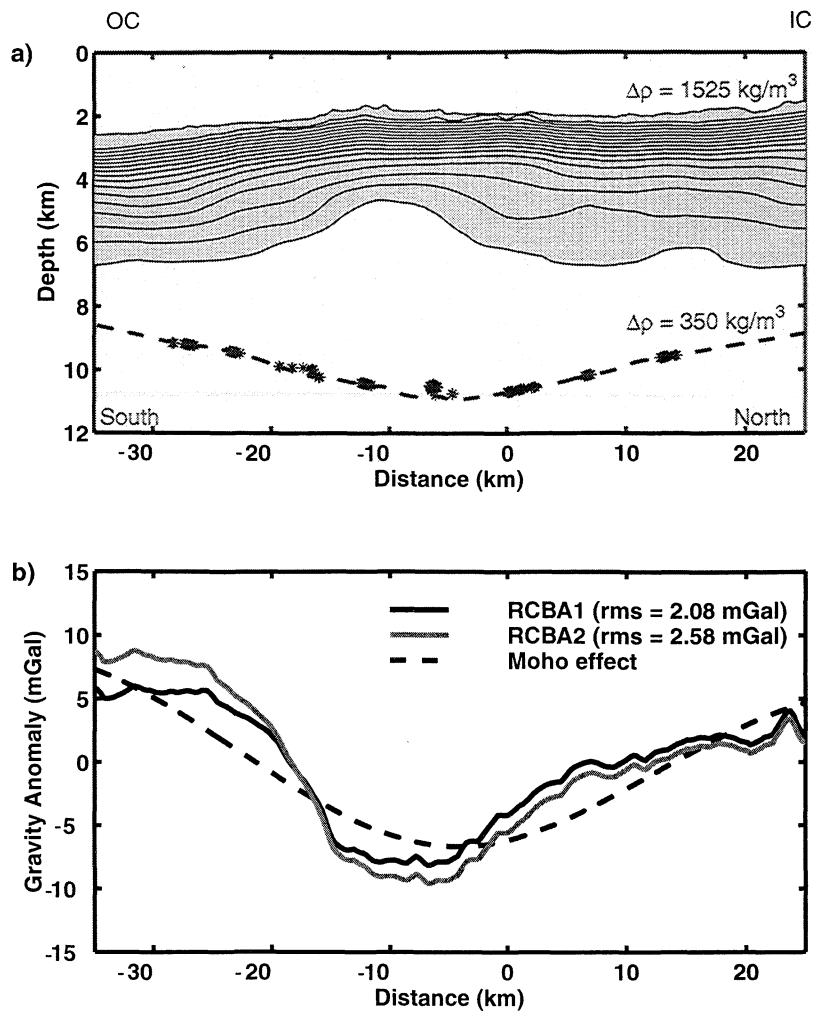
Figure 6. (a) Density model used to obtain the observed residual crustal Bouguer anomaly (RCBA) for the crustal structure in Figure 3a. Velocity contours were extracted from the velocity model at 0.1 km/s intervals from the seafloor to the 7 km/s contour and extended in three dimensions for the gravity calculation. We used a density contrast of 1525 kg/m³ across the seafloor and a density contrast of 350 kg/m³ across the Moho. (b) Observed (solid lines) and predicted (dashed line) RCBA for the seismic result in Figure 3a. RCBA1 (solid line) was calculated using the velocity-density relation in the text and RCBA2 (shaded line) was calculated using (3) of *Carlson and Raskin* [1984]. VE = 3.1.

line, we extended the Moho on either side by assuming a constant gradient in crustal thickness variation; this is a reasonable assumption considering the crustal thickness for the eastern rift mountains determined by *Sinha and Louden* [1983]. Similar to the results of *Hooft et al.* [2000], the calculated effect of the Moho topography accounts for most of the RCBA amplitude (Figure 6b, dotted line), although the predicted Moho effect is more gradual than the observed RCBA. The remaining anomaly therefore probably results from unmodeled density variations in the shallowmost crust (layer 2A), lower crust, and upper mantle or from uncertainties in the determination of the seismic Moho.

7. Interpretation and Discussion

The ridge-parallel seismic studies at segment OH-1 provide a record of spatial variations in crustal accretion and evolution at the slow-spreading MAR over the last 2 m.y. Detailed discussions on the western rift mountain and the axial valley experiments are given by *Canales et al.* [2000] and *Hooft et al.* [2000], respectively. Here we provide a joint

interpretation of the results of all three OH-1 refraction lines from the MARBE cruise.

Plate 1 and Figure 7 present the crustal velocity structure and thickness beneath the western rift mountains (Line W, Plate 1a), axial valley (Line C, Plate 1b), and eastern rift mountains (Line E, Plate 1c) over the region of common coverage (see Figure 1a). To compare the velocity structures along Lines W and C, which were obtained using the *Toomey et al.* [1994] tomography program (hereinafter referred to as the Toomey code), with the structure along Line E (obtained using the Korenaga code), we inverted the rift mountain data sets (Lines E and W) with both programs. The tests showed that the velocity models obtained for Line E using both methods were extremely similar. The same was true for Line W. Thus direct comparison of the three experiments is valid despite using different tomography algorithms.

Comparison of crustal thickness values from the three experiments is more complex. For Lines W and C, the PmP data were forward modeled using the algorithm of *Zelt and Smith* [1992] after first determining the seismic velocity structure using the Toomey code. This two-step procedure
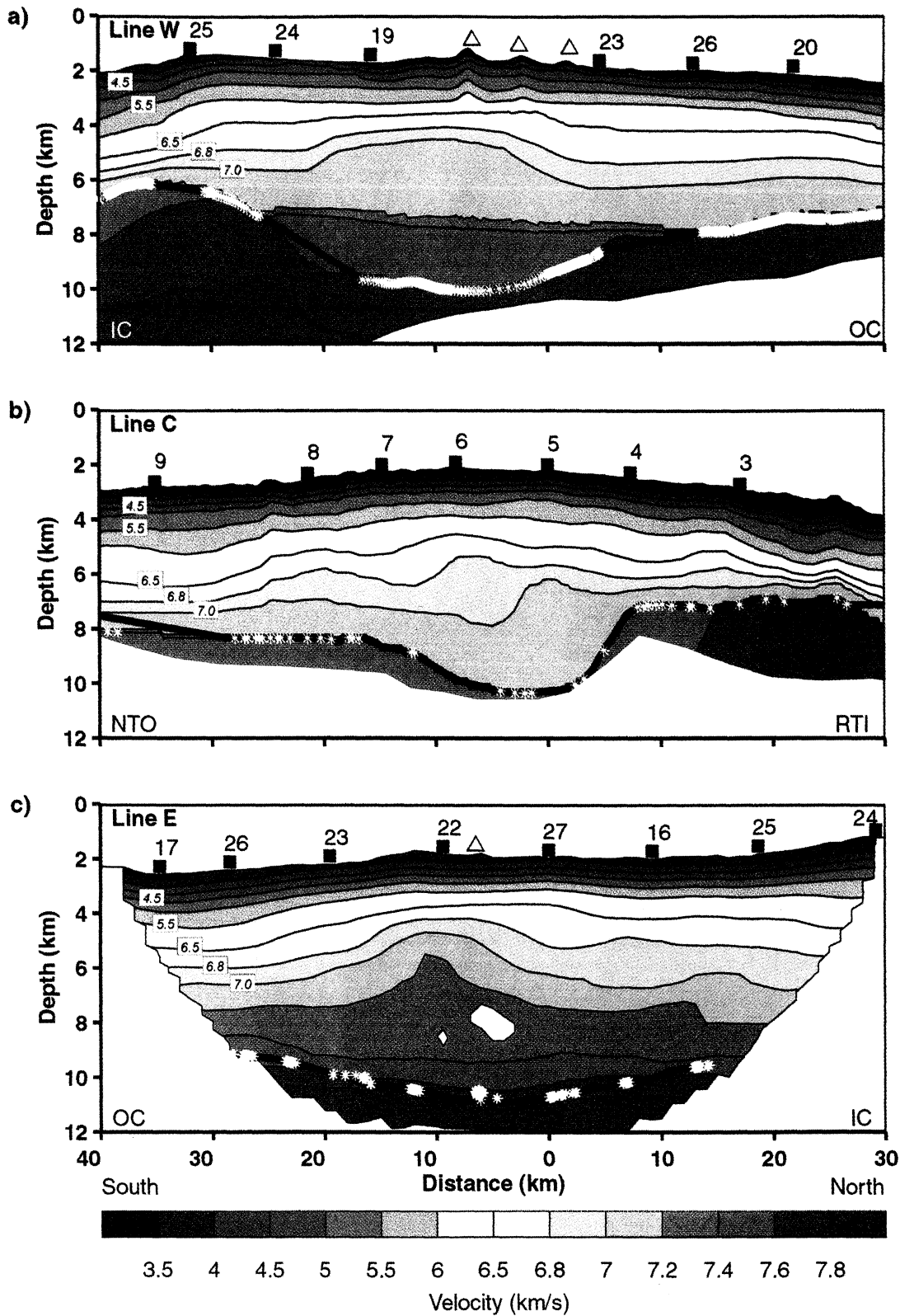
Plate 1. Final P wave velocity models for the (a) western rift mountains (Line W), (b) axial valley (Line C), and (c) eastern rift mountains (Line E) of OH-1 (see Figure 1 for line locations). Both Lines W and C image 2 m.y. old crust. PmP reflection points are denoted by white stars, which define the seismic Moho along the lines. Note that the contour interval is 0.5 km/s between 3.0 and 6.5 km/s and 0.2 km/s between 6.8 and 7.8 km/s Coordinates for Line C are the same as by *Hooft et al.* [2000]. Coordinates for Line W correspond to coordinates 18-88 of *Canales et al.* [2000]. See Figure 1a for position of x=0 on Lines W and C; on Line E, x=0 corresponds to OBH 27. The RMS travel time residual for each tomographic solution was 31 ms (Line W), 26 ms (Line C), and 30 ms (Line E). Solid squares and open triangles are as in Figure 3. VE = 2.4.
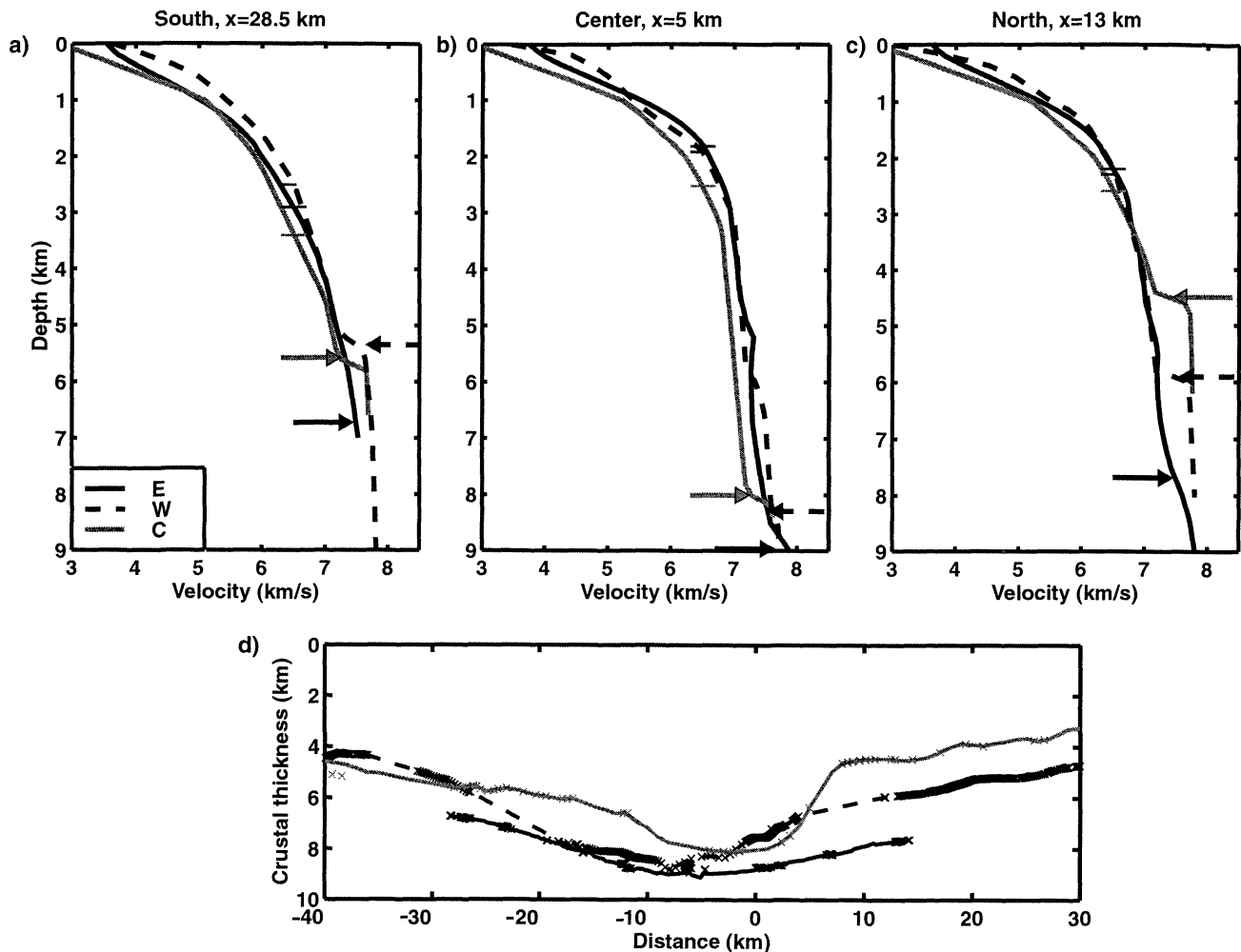
Figure 7. Velocity-depth profiles extracted from the two-dimensional tomographic images in Plate 1 at (a) the south end (x=-28 km), (b) the center (x=-5 km), and (c) toward the north end (x=13) of OH-1. The solid line corresponds to Line E, the dashed line corresponds to Line W, and the shaded line corresponds to Line C. All depths are relative to the seafloor. Arrows indicate Moho depth at each profile location for each line. Short thin lines indicate the depth to the 6.5 km/s contour, defined as the boundary between the upper and lower crust. (d) Crustal thicknesses along all three lines, using the same line styles as in Figures 7a-c. Crosses denote PmP reflection points.

was necessary because in the Toomey code the ray tracer models only refracted phases. In contrast, the Korenaga code inverts refracted and reflected phases jointly. We used this newer method to analyze Line E to minimize errors which may have resulted from using inconsistent parameterizations for velocity structure and Moho depth modeling for Lines W and C. To test the effects of different methodologies on the crustal thickness solutions, we inverted the Line W data set using the Korenaga code and compared the results to that of *Canales et al.* [2000], which were obtained using the Toomey code and *Zelt and Smith* [1992]. The inverted Moho for Line W using the Korenaga code differed only slightly from the Moho determined using *Zelt and Smith* [1992] (Plate 1a), indicating that the methodology used to determine crustal thickness does not strongly affect the final result.

An unaccounted-for source of error in the results presented here, however, is the effect of three-dimensional ray sampling, or out-of-plane propagation, in the three ray sets. In the case of significant across-axis structure, such as through-going crustal faulting or large-scale lateral variations in Moho depth, two-dimensional analysis of the three ridge-parallel

lines may introduce error into the results. Recent numerical experiments that incorporate realistic 2-D and 3-D source-receiver geometries, though, suggest that out-of-plane effects are relatively small, with errors in crustal velocity up to 0.15 km/s and errors in depth up to 2 km [*Zelt and Zelt*, 1998]. These values approximate the uncertainties derived from the travel time inversion; thus we assume that out-of-plane effects do not significantly affect comparisons of the three isochron-parallel seismic lines.

7.1. Evolution of Velocity Structure With Age

7.1.1. Upper crust. The thickness of the upper crust or seismic layer 2, defined as the depth to the 6.5 km/s contour, varies along the strike of each OH-1 refraction line, with generally the thickest upper crust at the segment ends and the thinnest upper crust at the segment center (Plate 1). On axis, the mean thickness of layer 2 is 2.9 km. In contrast, the mean upper crustal thickness beneath both flanks on 2 m.y. old crust is 2.3 km, significantly thinner than beneath the rift valley. The mean velocity of the upper crust differs in each

setting as well, with a value of 4.5 km/s on axis and 5.2-5.3 km/s off axis, an increase of 16%.

This observation of increasing seismic velocity in the upper crust with age is consistent with other studies which showed a rapid increase in the velocity of seismic layer 2A in crustal ages from 0 to 5 m.y. [*Carlson*, 1998]. Although we cannot distinguish layer 2A from layer 2B in the OH-1 refraction data, the observed increase in seismic velocity with age may actually reflect variations in layer 2A velocity since other seismic studies indicate little age dependence of layer 2B velocity at the MAR and EPR [*Carlson*, 1998] and at the ultraslow spreading Mohns Ridge [*Klingelhofer et al.*, 2000]. Some variability does exist in the thickness and mean velocity of layer 2A at OH-1. In the western rift mountains, for example, MCS images show that layer 2A thickens by 150 m from the center of the segment to its northern end [*Hussenoeder*, 1998]. Similarly, at two locations on the eastern flank, the velocity of the upper 50 m of crust varies by 20% over an along-strike distance of only 5 km. Such along- and across-strike variability suggests that the relationship between upper crustal structure and age at OH-1 is complex and probably dependent on numerous factors, including porosity, shallow along-axis melt migration, alteration, and tectonic modification.

7.1.2. Middle and lower crust and upper mantle. The middle to lower crust on all three OH-1 seismic lines is characterized by the typical low velocity gradients of seismic layer 3 (<1.0 s^{-1}) (Figure 7): between the base of the upper crust and the Moho, velocities increase from 6.5 km/s to 7.6 km/s over a depth of 2-6 km. However, the thickness of layer 3 varies considerably along the strike of each line, with the thickest layer 3 at the segment center and the thinnest layer 3 at the distal ends (Plate 1). This result is similar to that observed at the rift valley on the MAR at 33°S [*Tolstoy et al.*, 1993].

In contrast to the observed along-strike variation in layer 3 thickness, the average velocity in layer 3 changes very little along each line. Further, the average lower crustal velocities are nearly indistinguishable on Lines E and W and from that of the on axis line, except at the segment center where layer 3 velocities are 0.5 km/s lower on axis than on the flanks (Figure 7b). *Magde et al.* [2000] also imaged relatively low velocities (-0.4 km/s) in the middle to lower crust beneath the rift valley of OH-1. They attributed these lower layer 3 velocities to elevated temperatures and the presence of partial melt. A similar difference in mean layer 3 velocity of zero-age and older crust was observed near the Kane fracture zone, where *Purdy and Detrick* [1986] found layer 3 velocities on axis to be 0.4 km/s slower than in 7 m.y. old crust.

7.1.3. Upper mantle. The limited number of *Pn* arrivals on the rift valley and eastern rift mountain lines precludes a detailed comparison of upper mantle structure beneath the three OH-1 lines. We note, however, that an upper mantle velocity of 7.8 km/s is observed on both off-axis lines beneath at least the central 30 km of OH-1 (Plates 1a and 1c). Beneath the rift valley the mantle velocity is 0.4 km/s slower, except in the immediate vicinity of the Oceanographer fracture zone (Plate 1b). The higher mantle velocity off axis may be partly caused by cooling of the upper mantle with time and/or the solidification of partial melt.

7.2. Low-Velocity Anomalies in the Mid-Crust Near Segment Ends

Although the images of absolute velocity shown in Plate 1 illustrate well the large-scale structure along the OH-1 refraction lines, smaller-scale crustal heterogeneity is better emphasized by the deviation of the observed absolute velocities from a reference 1-D model. Plate 2 shows the difference between the observed absolute velocities and the 1-D velocity-depth profile from the segment midpoint of Line C, which was used as the starting model for the Line E inversion. The most striking features in these velocity perturbation plots are the relatively low velocities at both ends of Lines C and E and at the southern end of Line W.

Anomalous crustal structure at segment ends is a common observation at MAR fracture zones [*Detrick and Purdy*, 1980; *Sinha and Louden*, 1983; *Cormier et al.*, 1984; *Ambos and Hussong*, 1986; *Louden et al.*, 1986; *Detrick et al.*, 1993]; within the fracture zone valley itself, seismic layer 3 typically thins by several kilometers or disappears entirely, and the total crustal thickness can be as low as 2 km. Several mechanisms may be responsible for these observations, including fracturing and alteration, restricted melt supply due to the large distance from segment-centered mantle upwelling, reduced in situ melting due to the thermal edge effect of adjacent cold lithosphere, and serpentinization of mantle peridotite. The magnitude of the observed variations in crustal velocities and thicknesses, however, vary significantly at MAR fracture zones, and the crust near the Oceanographer fracture zone in particular exhibits normal properties except within the fracture zone valley itself [*Sinha and Louden*, 1983; *Ambos and Hussong*, 1986]. A similar abrupt transition from normal thickness crust along strike to thinned crust in the fracture zone is also observed at the Kane fracture zone [*Detrick and Purdy*, 1980].

The mechanisms responsible for the large zones of low velocities at the distal ends of OH-1 are probably similar to those which are cited to alter fracture zone crust. In particular, the reduced shallow crust and mid-crust *P* wave velocities at segment ends may result from serpentinization of mantle peridotite, fracturing and alteration, or a combination of these effects. Although we cannot rule out the presence of serpentinized mantle at the segment ends of OH-1, a detailed analysis of the inferred density structure along Line W by *Canales et al.* [2000] suggests that serpentinization is likely restricted to the valley of the NTO and does not extend into the neighboring ridge segments. We believe instead that the large low-velocity regions at the distal ends of OH-1 result from fracturing and cracking of newly accreted crust that is already somewhat thin due to attenuated melt supply. Abundant surface faults observed in the bathymetry map (Figure 1a) suggest that faulting significantly modifies newly formed crust as it is uplifted from the rift valley into the flanking crestal mountains. The inference of pervasive faulting at the ends of OH-1 is consistent with the observation that microearthquake activity is found at the inside corners of both the NTO and Oceanographer fracture zone [*Barclay et al.*, 2001]. However, inside corner tectonism does not explain the presence of the low-velocity region at the southern end of Line E, which is located at an outside corner. This particular low-velocity anomaly may result from tectonism associated with the southward propagation of OH-1 since the southern end of Line E intersects the disturbed crust of the propagation wake.

7.3. High-Velocity Anomalies in Mid-Crust Beneath Seamounts

The western and eastern rift mountains have similar mid-crustal velocity structures. A significant common feature is the presence of ~7% higher than average velocities at 3-5 km depth at the segment midpoint (Plates 1a, 1c, 2a and 2c). On Line E this high-velocity anomaly lies between three seamounts adjacent to the refraction line (Figure 1c), and on Line W it occurs immediately beneath three line-centered seamounts (Figure 1b). Detection of high velocities beneath subaerial volcanoes is common. For example, a tomography
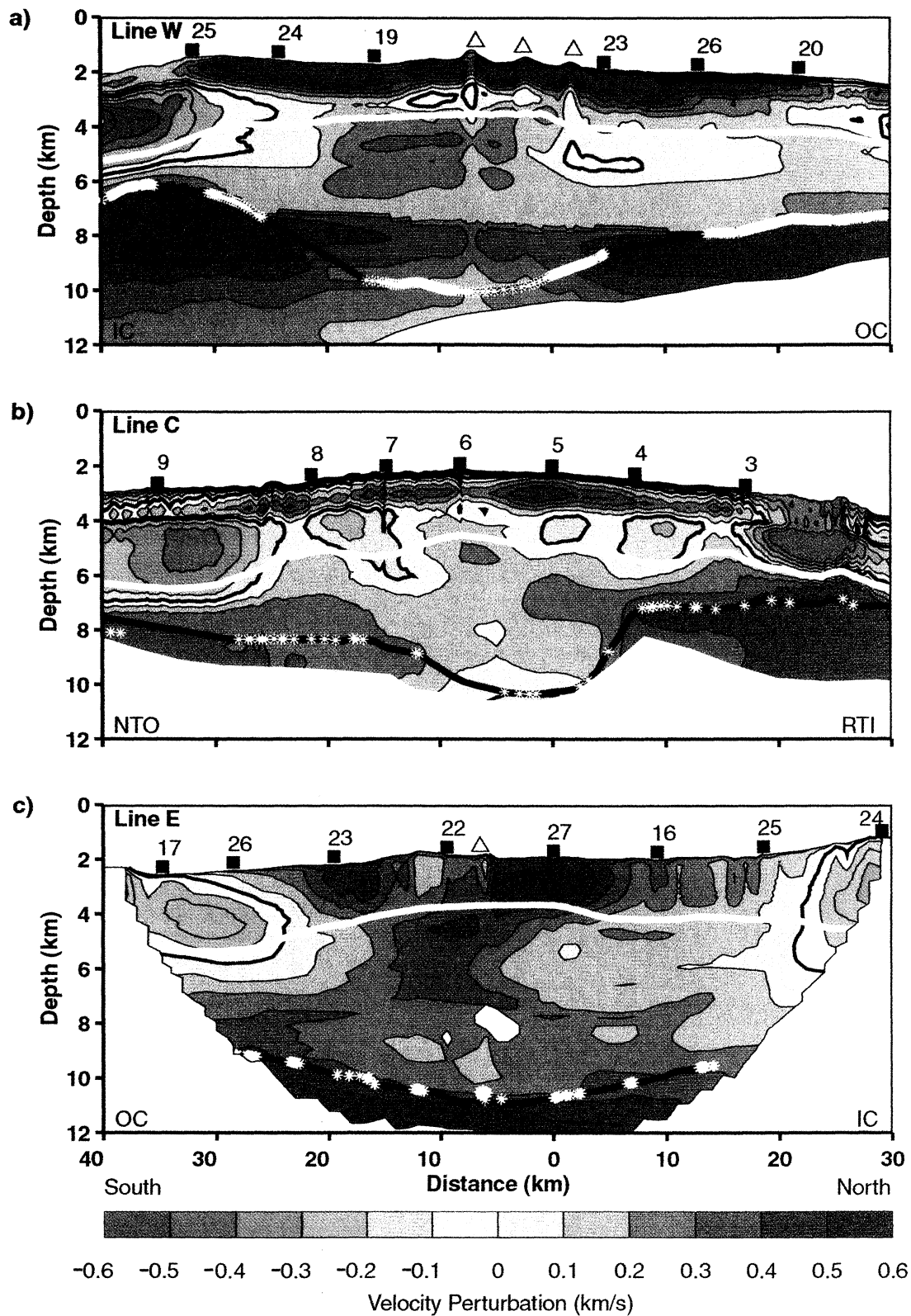
Plate 2. Difference between the *P* wave velocity models in Plate 1 and an average velocity-depth profile from the central axial valley of OH-1 for (a) Line W, (b) Line C, and (c) Line E. White solid line on each panel denotes the boundary between the upper and lower crust (6.5 km/s contour in Plate 1). Solid squares and open triangles are as in Figure 3. VE = 2.4.

experiment at the Hengill complex in southwestern Iceland imaged four regions of elevated velocities, three of which occurred directly beneath volcanoes [*Foulger and Toomey*, 1989]. In particular, the Husmuli volcano, which resembles the size of many of the OH-1 seamounts, is underlain by a high-velocity body with a depth (4 km) and magnitude (+7%) similar to the body imaged beneath the eastern rift mountains. The major difference between the two anomalies is in their aspect ratios: the Husmuli feature is tall and narrow, while the anomaly we image is short and wide.

Following the conclusion of *Foulger and Toomey* [1989], we hypothesize that the high-velocity bodies imaged beneath the seamounts at OH-1 may be volcanic "roots" consisting of relatively unfractured intrusions or solidified magma chambers of the volcanoes. The volume of the root beneath Line E is calculated by multiplying its along-axis length (6.5 km), depth (2 km), and cross-axis width (3 km); this latter number was determined by a 3-D MARBE experiment centered on the OH-1 rift valley [*Magde et al.*, 2000]. Assuming the root has a rectangular cross section, its volume is 39 km^3, which is a factor of 2 larger than the 15-20 km^3 volume estimated for the anomaly beneath the Husmuli volcano [*Foulger and Toomey*, 1989]. However, because several seamounts lie adjacent to Line E, this large volume may be the sum of individual roots beneath each volcano.

The shape and velocity contrast of these high-velocity bodies are not sufficient to produce observable seismic reflections as might be recorded in multichannel seismic data. Similarly, the density contrast between the intrusions and the surrounding crust is too small to produce a noticeable gravity anomaly at the sea surface. However, based on the common occurrence of the volcanic roots on Lines E and W, similar high-velocity intrusions may underlie many if not all of the off axis OH-1 seamounts.

An unusual feature of the velocity images from the two rift mountain lines is the apparent thinning of seismic layer 2 immediately beneath the seamounts (Plate 1 and Figure 7b). It is interesting to note that ~3 km east of Line E, MCS analysis at two locations shows that layer 2A is 275 m thinner at a site closest to a particularly large seamount [*Hussenoeder*, 1998]. A reduction in the volume of extrusive material beneath a volcano is counterintuitive. The most likely scenario is that the extrusive section beneath the seamounts is denser than the surrounding shallow crust, thereby increasing the seismic velocity and making layer 2 appear thinner. Increased densities could result from a more massive and less fractured extrusive section beneath the seamount relative to the surrounding extrusives or from a mixture of normal-density extrusive material with higher-density feeder dikes associated with the volcano. *Cochran et al.* [1999] invoke both of these factors to explain observed density differences within layer 2A at the EPR. Apparent thinning of layer 2 was not observed beneath the rift valley line (Plate 1b), potentially because of the counter-effects of low-density partial melt and higher temperatures within the axial upper crust [*Barclay et al.*, 1998] and because the line did not directly cross a seamount. Future near-bottom gravity measurements would be one way to test if shallow crustal densities near the OH-1 seamounts are indeed higher than the density of the surrounding extrusive crust.

7.4. Anomalous Crustal Thickness of the OH-1 Segment

Figure 7d shows crustal thicknesses for all three OH-1 refraction lines over the region of common coverage. Each line is underlain by very thick crust near the segment center (x=-5 km), with maximum thicknesses of 8.1 km on axis and 9 km off axis. These maximum values are 1-2 km larger than observed at OH-2 and OH-3, immediately to the south

[*Canales et al.*, 2000; *Hooft et al.*, 2000]. They also lie at the top end of the observed range of seismic crustal thickness measurements at ridges that are unaffected by hotspots [*White et al.*, 1992; *Bown and White*, 1994].

The seamount chain centered on OH-1 is often cited as evidence for a high magma budget [e.g., *Gràcia et al.*, 1999]. However, the seismic results in Plate 2 show that the inferred crustal magma bodies that underlie the seamounts are localized features with small volumes. Thus these small magma sources probably do not contribute significant volumes of melt to build the thick crustal roots at the segment center. Two main classes of models are commonly invoked to explain crustal thickness variations at slow spreading ridges. In the first model the mantle rises as a focused diapir beneath the center of an individual ridge segment. Because the diapir is hotter and more buoyant at its center than at its edges, decompression melting is enhanced in the core of the diapir, thereby creating thicker crust at the segment center than at either end [*Kuo and Forsyth*, 1988; *Lin et al.*, 1990]. This model explains well the observation of circular MBA lows observed at the MAR. In the second model the mantle also rises vertically beneath a ridge segment, but melt production is constant along strike. The thick crust at the segment center results not from a larger extent of partial melting but rather from efficient migration of melt away from the segment ends toward the segment center [*Magde and Sparks*, 1997; *Magde et al.*, 1997].

Hooft et al. [2000] suggest that the thick crust at the center of OH-1 results from efficient transport of melt along paths defined by steep mantle isotherms associated with the large-offset Oceanographer fracture zone. This conclusion seems to support the model where lateral variations in melt delivery explain crustal thickness variations. However, new geochemical analyses of lavas at OH-1 show that the mantle beneath the segment center is enriched in incompatible elements, total alkalis, and H$_2$O content [*Niu et al.*, 2001], and thus likely melts extensively. *Niu et al.* [2001] thus support the mantle diapir model with the caveat that heterogeneous mantle composition is a critical variable governing crustal accretion at slow spreading ridges.

The three ridge-parallel seismic experiments at OH-1 show that while the large-scale crustal velocity structure of the crust has remained relatively constant over the last 2 m.y., significant differences in crustal thickness exist. In particular, north of the segment center the crust is 4 km thicker beneath the eastern rift mountains relative to the rift valley and 2 km thicker relative to the conjugate western rift mountains (Figure 7d). We suggest that this pattern results from two possible scenarios. In the first scenario the crust beneath the rift mountains may have formed during a period of mantle melting in which the average melt production was greater than it is today. Based on the observation of alternating high- and low-amplitude residual gravity anomalies at 25°-27°N on the MAR, *Tucholke et al.* [1997] estimate that the formation of buoyant melt diapirs and/or mantle heterogeneities occurs over a 2-3 m.y. cycle. If we assume that the effect of the Oceanographer fracture zone on the thermal state of the segment has remained relatively constant during the last 2 m.y., the along-strike variation in crustal thickness we observe between the rift valley and rift mountains lines must derive from variable melt production instead of from variable melt delivery. Although we cannot rule out the contribution of 3-D melt delivery in building the crust at OH-1, our results together with those of *Niu et al.* [2001] are more compatible with the focused mantle upwelling model to explain crustal thickness variations at OH-1.

On the other hand, the differences in crustal thickness observed at OH-1 may derive simply from asymmetric

modification after the crust formed, with preferential thinning on the western flank upon uplift from the rift valley. This asymmetry may result from differences in the three-dimensional fault geometry on each flank and by variations in crustal accretion; Figure 1a shows that Line W lies on a topographic high, while Line E is located along a wide plateau. In addition, the southern end of Line W may be especially thinned due to the combined effects of an NTO inside corner and the southward propagation of the OH-1 segment.

8. Conclusions

From a joint interpretation of seismic and gravity data collected in the western rift mountains, rift valley, and eastern rift mountains at MAR segment OH-1 we conclude the following:

1. The mean upper crustal (layer 2) velocity increases 16% from 4.5 km/s on axis to 5.2 km/s on 2 m.y. old crust on each flank. This increase in shallow crustal velocity off axis may reflect fissure sealing and mineral alteration primarily within layer 2A as the crust ages. The mean thickness of the upper layer decreases 20% over the same time span, from 2.9 to 2.3 km. In both on axis and off axis settings the upper crust is thinner at the segment center than at the segment ends. The mean lower crustal (layer 3) velocities are very similar for 0 and 2 m.y. old crust, except for a small low velocity anomaly on axis interpreted as elevated temperatures and/or partial melt. In all three settings layer 3 is thicker at the segment center than it is at the segment ends. The mantle velocity is 7.4 km/s beneath the rift valley and 7.8 km/s beneath either flank. The higher off-axis mantle velocities probably result from cooling of the mantle with time and/or the solidification of partial melt.

2. The maximum crustal thickness is 8-9 km beneath the center of all three seismic lines; this is at the high end of the seismic crustal thickness measurements for the MAR. The crust thins by 5 km toward the ends of the rift valley, by 4 km toward the ends of the western rift mountains, and by 2 km toward the ends of the eastern rift mountains. The Moho is as much as 2 km deeper beneath the eastern flank than beneath the conjugate western flank, despite their similar age. This large difference may derive from asymmetric post emplacement modification related to differences in fault geometry on each flank. Additionally, the southern end of the western line may be particularly thinned by the tectonic processes associated with the southward propagation of the segment.

3. Large regions (10-15 km wide, 4 km deep) of relatively low velocities (-0.1 to 0.5 km/s) are imaged at both ends of the rift valley, both ends of the eastern rift mountains, and the southern end of the western rift mountains. These lowered values may be caused by fracturing facilitated by the greater tectonic deformation at segments ends and by the southward propagation of OH-1.

4. A mid-crust high-velocity body is spatially associated with clusters of large seamounts in the western and eastern rift mountains. We suggest that each body consists of a relatively unfractured volcanic root or the solidified magma chamber which fed the overlying seamounts. The upper crust thins by 500 m above these high-velocity anomalies, possibly indicating relatively higher densities in the extrusive section relative to the surrounding upper crust. These higher densities may result from a less fractured extrusive section beneath the seamounts or from a mixture of normal density basalt and higher density feeder dikes. Based on the relatively small size of these roots, volcanism associated with the seamounts probably does not contribute substantially to the thickened crust at the center of the segment.

References

Ambos, E.L., and D.M. Hussong, Oceanographer transform fault structure compared to that of surrounding oceanic crust: Results from seismic refraction data analysis, *J. Geodyn.*, 5, 79-102, 1986.

Barclay, A.H., D.R. Toomey, and S.C. Solomon, Seismic structure and crustal magmatism at the Mid-Atlantic Ridge, 35°N, *J. Geophys. Res.*, *103*, 17,827-17,844, 1998.

Barclay, A.H., D.R. Toomey, and S.C. Solomon, Microearthquake characteristics and crustal Vp/Vs structure at the Mid-Atlantic Ridge, 35°N, *J. Geophys. Res.*, *106*, 2017-2034, 2001.

Bown, J.W., and R.S. White, Variation with spreading rate of oceanic crustal thickness and geochemistry, *Earth Planet. Sci. Lett.*, *121*, 435-449, 1994.

Brozena, J.M., Temporal and spatial variability of seafloor spreading processes in the northern South Atlantic, *J. Geophys. Res.*, *91*, 497-510, 1986.

Bryan, W.B., S.E. Humphris, G. Thompson, and J.F. Casey, Comparative volcanology of small axial eruptive centers in the MARK area, *J. Geophys. Res.*, *99*, 2973-2984, 1994.

Canales, J.P., R.S. Detrick, J. Lin, J.A. Collins, and D.R. Toomey, Crustal and upper mantle seismic structure beneath the rift mountains and across a non-transform offset at the Mid-Atlantic Ridge (35°N), *J. Geophys. Res.*, *105*, 2699-2719, 2000.

Carbotte, S., S.M. Welch, and K.C. Macdonald, Spreading rates, rift propagation, and fracture zone offset histories during the past 5 my on the Mid-Atlantic Ridge; 25°-27°30' S and 31°-34°30' S, *Mar. Geophys. Res.*, *13*, 51-80, 1991.

Caress, D.W., M.S. Burnett, and J.A. Orcutt, Tomographic image of the axial low-velocity zone at 12°50'N on the East Pacific Rise, *J. Geophys. Res.*, *97*, 9243-9263, 1992.

Carlson, R.L., Seismic velocities in the uppermost oceanic crust: Age dependence and the fate of layer 2A, *J. Geophys. Res.*, *103*, 7069-7077, 1998.

Carlson, R.L., and G.S. Raskin, Density of the ocean crust, *Nature*, *311*, 555-558, 1984.

Cochran, J.R., D.J. Fornari, B.J. Coakley, R. Herr, and M.A. Tivey, Continuous near-bottom gravity measurements made with a BGM-3 gravimeter in DSV *Alvin* on the East Pacific Rise crest near 9°31'N and 9°50'N, *J. Geophys. Res.*, *104*, 10,841-10,861, 1999.

Cormier, M.-H., R.S. Detrick, and G.M. Purdy, Anomalously thin crust in oceanic fracture zones: New seismic constraints from the Kane fracture zone, *J. Geophys. Res.*, *89*, 10,249-10,266, 1984.

Creager, K.C., and L.M. Dorman, Location of instruments on the seafloor by joint adjustment of instrument and ship positions, *J. Geophys. Res.*, *87*, 8379-8388, 1982.

DeMets, C., R.G. Gordon, D.F. Argus, and S. Stein, Current plate motions, *Geophys. J. Int.*, *101*, 425-478, 1990.

Deplus, C., et al., Linking variation in magma supply and segment growth: temporal evolution of segment OH-1 (MAR at 35°N) during the last 12 Myr, *Eos Trans. AGU*, *69*(44), Fall Meet. Suppl., F856, 1998.

Detrick, R.S., Jr., and G.M. Purdy, The crustal structure of the Kane fracture zone from seismic refraction studies, *J. Geophys. Res.*, *85*, 3759-3777, 1980.

Detrick, R.S., R.S. White, and G.M. Purdy, Crustal structure of North Atlantic fracture zones, *Rev. Geophys.*, *31*, 439-458, 1993.

Detrick, R.S., H.D. Needham, and V. Renard, Gravity anomalies and crustal thickness variations along the Mid-Atlantic Ridge between 33°N and 40°N, *J. Geophys. Res.*, *100*, 3767-3787, 1995.

Escartín, J., and J. Lin, Ridge offsets, normal faulting, and gravity anomalies of slow spreading ridges, *J. Geophys. Res.*, *100*, 6163-6177, 1995.

Foulger, G.R., and D.R. Toomey, Structure and evolution of the Hengill-Grensdalur volcanic complex, Iceland: Geology, geophysics, and seismic tomography, *J. Geophys. Res.*, *94*, 17,511-17,522, 1989.

Fox, P. J., E. Schreiber, H. Rowlett, and K. McCamy, The geology of the Oceanographer fracture zone: A model for fracture zones, *J. Geophys. Res.*, *81*, 4117-4128, 1976.

Gente, P., G. Ceuleneer, C. Durand, R. Pockalny, and M. Maia, Propagation rate of segments along the Mid-Atlantic Ridge between 20° and 24° (SEADMA I cruise), *Eos Trans. AGU*, *73*(43), Fall Meet. Suppl., F569, 1992.

Gràcia, E., D. Bideau, R. Hekinian, and Y. Lagabrielle, Detailed geologic mapping of two second-order segments of the Mid-Atlantic Ridge between Oceanographer and Hayes fracture zones (33°30'N-35°N), *J. Geophys. Res.*, *104*, 22,903-22,921, 1999.

Hooft, E.E.E., R.S. Detrick, D.R. Toomey, J.A. Collins, and J. Lin, Crustal thickness and structure along three contrasting spreading segments of the Mid-Atlantic Ridge, 33.5°-35°N, *J. Geophys. Res.*, *105*, 8205-8226, 2000.

Hussenoeder, S.A., Seismic and magnetic constraints on the structure of upper oceanic crust at fast and slow spreading ridges, Ph. D. thesis, Woods Hole Oceanogr. Inst./Mass. Inst. of Technol. Joint Program, Woods Hole, 1998.

Jaroslow, G.E., D.K. Smith, and B.E. Tucholke, Record of seamount production and off-axis evolution in the western North Atlantic Ocean, 25°25'-27°10'N, *J. Geophys. Res.*, *105*, 2721-2736, 2000.

Klingelhofer, F., L. Geli, L. Matias, N. Steinsland, and J. Mohr, Crustal structure of a super-slow spreading centre: A seismic refraction study of Mohns Ridge, 72°N, *Geophys. J. Int.*, *141*, 509-526, 2000.

Korenaga, J., W.S. Holbrook, G.M. Kent, P.B. Keleman, R.S. Detrick, H.-C. Larsen, J.R. Hopper, and T. Dahl-Jensen, Crustal structure of the southeast Greenland margin from joint refraction and reflection seismic tomography, *J. Geophys. Res.*, *105*, 21,591-21,614, 2000.

Kuo, B.-Y., and D.W. Forsyth, Gravity anomalies of the ridge-transform system in the South Atlantic between 31 and 34.5°S: Upwelling centers and variations in crustal thickness, *Mar. Geophys. Res.*, *10*, 205-232, 1988.

Lin, J., G.M. Purdy, H. Schouten, and J.-C. Sempéré, Evidence from gravity data for focused magmatic accretion along the Mid-Atlantic Ridge, *Nature*, *344*, 627-632, 1990.

Louden, K.E., R.S. White, C.G. Potts, and D.W. Forsyth, Structure and seismotectonics of the Vema Fracture Zone, Atlantic Ocean, *J. Geol. Soc. London*, *143*, 795-805, 1986.

Magde, L.S., and D.W. Sparks, Three-dimensional mantle upwelling, melt generation and melt migration beneath segmented slow-spreading ridges, *J. Geophys. Res.*, *102*, 20,571-20,583, 1997.

Magde, L.S., D.W. Sparks, and R.S. Detrick, The relationship between buoyant mantle flow, melt migration, and gravity bull's eyes at the Mid-Atlantic Ridge between 33°N and 35°N, *Earth Planet. Sci. Lett.*, *148*, 59-67, 1997.

Magde, L.S., A.H. Barclay, D.R. Toomey, R.S. Detrick, and J.A. Collins, Crustal magma plumbing within a segment of the Mid-Atlantic Ridge, 35°N, *Earth Planet. Sci. Lett.*, *175*, 55-67, 2000.

McClain, J.S., and D.W. Caress, Seismic tomography in marine refraction experiments, in *Seismic Tomography: Theory and Practice*, edited by H.M. Iyer and K. Hirahara, pp. 764-780, Chapman and Hall, New York, 1993.

Moser, T.J., Shortest path calculations of seismic rays, *Geophysics*, *56*, 59-67, 1991.

Moser, T.J., G. Nolet, and R. Sneieder, Ray bending revisited, *Bull. Seismol. Soc. Am.*, *82*, 259-288, 1992.

Needham, H.D., M. Voisset, V. Renard, H. Bougault, O. Dauteuil, R. Detrick, and C. Langmuir, Structural and volcanic features of the Mid-Atlantic Rift Zone between 40°N and 33°N, *Eos Trans. AGU*, *73*(43), Fall Meet. Suppl., F552, 1992.

Niu, Y., D. Bideau, R. Hékinian, and R. Batiza, Mantle compositional control on the extent of mantle melting, crust production, gravity anomaly, ridge morphology, and ridge segmentation: A case study at the Mid-Atlantic Ridge 33-35°N, *Earth Planet. Sci. Lett.*, *186*, 383-399, 2001.

Parker, R.L., The rapid calculation of potential anomalies, *Geophys. J. R. Astron. Soc.*, *31*, 447-455, 1973.

Phipps Morgan, J., and D.W. Forsyth, Three-dimensional flow and temperature perturbations due to a transform offset: Effects on oceanic crustal and upper mantle structure, *J. Geophys. Res.*, *93*, 2955-2966, 1988.

Purdy, G.M., and R.S. Detrick, Crustal structure of the Mid-Atlantic Ridge at 23°N from seismic refraction studies, *J. Geophys. Res.*, *91*, 3739-3762, 1986.

Rabain, A., M. Cannat, J. Escartín, G. Pouliquen, C. Deplus, and C. Rommevaux-Jestin, Focused volcanism and growth of a slow spreading segment (Mid-Atlantic Ridge, 35°N), *Earth Planet. Sci. Lett.*, *185*, 211-224, 2001.

Schreiber, E., and P.J. Fox, Compressional wave velocities and mineralogy of fresh basalts from the Famous area and the Oceanographer fracture zone and the texture of layer 2A of the oceanic crust, *J. Geophys. Res.*, *81*, 4071-4076, 1976.

Severinghaus, J.P., and K.C. Macdonald, High inside corners at ridge-transform intersections, *Mar. Geophys. Res.*, *9*, 353-367, 1988.

Shirey, S.B., J.F. Bender, and C.H. Langmuir, Three-component isotopic heterogeneity near the Oceanographer transform, Mid-Atlantic Ridge, *Nature*, *325*, 217-223, 1987.

Sinha, M.C., and K.E. Louden, The Oceanographer fracture zone, 1, Crustal structure from seismic refraction studies, *Geophys. J. R. Astron. Soc.*, *75*, 713-736, 1983.

Smith, D.K., and J.R. Cann, Building the crust at the Mid-Atlantic Ridge, *Nature*, *365*, 707-715, 1993.

Smith, D.K., M.A. Tivey, H. Schouten, and J.R. Cann, Locating the spreading axis along 80 km of the Mid-Atlantic Ridge south of the Atlantis Transform, *J. Geophys. Res.*, *104*, 7599-7612, 1999.

Thibaud, R., P. Gente, and M. Maia, A systematic analysis of the Mid-Atlantic Ridge morphology and gravity between 15°N and 40°N: Constraints of the thermal structure, *J. Geophys. Res.*, *103*, 24,223-24,243, 1998.

Tolstoy, M., A.J. Harding, and J.A. Orcutt, Crustal thickness on the Mid-Atlantic Ridge: Bull's eye gravity anomalies and focused accretion, *Science*, *262*, 726-729, 1993.

Toomey, D.R., S.C. Solomon, and G.M. Purdy, Tomographic imaging of the shallow crustal structure of the East Pacific Rise at 9°30'N, *J. Geophys. Res.*, *99*, 24,135-24,157, 1994.

Tucholke, B.E., J. Lin, M.C. Kleinrock, M.A. Tivey, T.B. Reed, J. Goff, and G.E. Jaroslow, Segmentation and crustal structure of the western Mid-Atlantic Ridge flank, 25°25'-27°10'N and 0-29 m.y., *J. Geophys. Res.*, *102*, 10,203-10,223, 1997.

Van Avendonk, H.J.A., A.J. Harding, J.A. Orcutt, and J.S. McClain, A two-dimensional tomographic study of the Clipperton transform fault, *J. Geophys. Res.*, *103*, 17,885-17,899, 1998.

White, R.S., D. McKenzie, and R.K. O'Nions, Oceanic crustal thickness from seismic measurements and rare earth element inversions, *J. Geophys. Res.*, *97*, 19,683-19,715, 1992.

Yu, D., D. Fontignie, and J.-G. Schilling, Mantle plume-ridge interactions in the central North Atlantic: A Nd isotope study of Mid-Atlantic Ridge basalts from 30°N to 50°N, *Earth Planet. Sci. Lett.*, *146*, 259-272, 1997.

Zelt, C.A., and R.B. Smith, Seismic traveltime inversion for 2-D crustal velocity structure, *Geophys. J. Int.*, *108*, 16-34, 1992.

Zelt, C.A., and B.C. Zelt, Study of out-of-plane effects in the inversion of refraction/wide-angle reflection traveltimes, *Tectonophysics*, *286*, 209-221, 1998.

R.S. Detrick, A. Hosford, and J. Lin, Department of Geology and Geophysics, Woods Hole Oceanographic Institution, Woods Hole, MA 02543 (rdetrick@whoi.edu, allegra@mit.edu, jlin@whoi.edu.)